Check for updates

NANO · MICRO small
www.small-journal.com

Novel Polytype of III–VI Metal Chalcogenides Nano Crystals Realized in Epitaxially Grown InTe

Sangmin Lee, Young-Kyun Kwon, Miyoung Kim, and Gyu-Chul Yi**

III–VI metal chalcogenides have garnered considerable research attention as a novel group of layered van der Waals materials because of their exceptional physical properties and potential technological applications. Here, the epitaxial growth and stacking sequences of InTe is reported, an essential and intriguing material from III–VI metal chalcogenides. Aberration-corrected scanning transmission electron microscopy (STEM) is utilized to directly reveal the interlayer stacking modes and atomic structure, leading to a discussion of a new polytype. Furthermore, correlations between the stacking sequences and interlayer distances are substantiated by atomic-resolution STEM analysis, which offers evidence for strong interlayer coupling of the new polytype. It is proposed that layer-by-layer deposition is responsible for the formation of the unconventional stacking order, which is supported by ab initio density functional theory calculations. The results thus establish molecular beam epitaxy as a viable approach for synthesizing novel polytypes. The experimental validation of the InTe polytype here expands the family of materials in the III–VI metal chalcogenides while suggesting the possibility of new stacking sequences for known materials in this system.

1. Introduction

The unique and intriguing physical properties of van der Waals (vdW) layered materials have been the subject of extensive research. One of the most interesting aspects of these layered materials is that their properties are often influenced by the properties of individual layers and by factors, such as thickness and stacking order.[1–4] Even when the constituent layers are identical, various stacking orders exist because of the different relative orientations and atomic alignments between the layers, leading to diverse polytypes. Distinction between various polytypes in layered materials is a key consideration because many physical properties depend on the polytype. For instance, the stacking order plays a key role in controlling optical properties, such as bandgap tunability and second harmonic generation.[5–8] Therefore, the diverse phase of vdW layered materials hosts rich physics; it is important to demonstrate their different polytypes as characterized by distinct stacking sequences of the layers.

Layered III–VI metal chalcogenides have emerged as a promising new vdWsystem due to their excellent physical and chemical properties, with potential applications in photonics, solar energy conversion, and photocatalysis.[4,7,9–15] Particularly, recent research has highlighted the exceptional second-order nonlinearity of layered III–VI metal chalcogenides, which heavily relies on the layered arrangement; thus, it is a unique vdW system in terms of nonlinear response.[4,11,16] Despite extensive researches on GaS, GaSe, and InSe,[16–18] vdW layered indium telluride (InTe) has received comparatively less attention. There are only a few theoretical investigations and reports of epitaxial growth of vdW layered InTe using alternative vdW materials as substrates.[19–21] This is attributed to the indium and tellurium compounds' ability to crystallize in diverse structures and oxidation states, particularly challenging due to the less favorable hexagonal phase in a vdW layered structure. Previous researches on bulk indium telluride, the cubic phase In_2Te_3 or tetragonal phase InTe, have mainly focused on their outstanding thermoelectric effects.[22–25] The structural flexibility offered by the vdW layered configuration may facilitate novel functionalities, distinguishing it from traditional 3D bulk materials. Indeed, because of the high atomic number in families III–VI on the periodic table and its strong spin-orbit coupling, vdW InTe may exhibit exotic physical properties, such as unconventional hidden Rashba effects and inverted band structures.[26] Moreover, vdW layered InTe has the smallest bandgap among layered III–VI family members, making it ideal for applications requiring an optical response in the infrared range.[19–21] Thus, there is a need to synthesize InTe and investigate its layered structure and

S. Lee, M. Kim
Department of Materials Science & Engineering and Research Institute of Advanced Materials
Seoul National University
Seoul 08826, Republic of Korea
E-mail: mkim@snu.ac.kr

Y.-K. Kwon
Department of Physics
Department of Information Display
and Research Institute for Basic Sciences
Kyung Hee University
Seoul 02447, South Korea

G.-C. Yi
Department of Physics and Astronomy
Seoul National University
Seoul 08826, Republic of Korea
E-mail: gcyi@snu.ac.kr

The ORCID identification number(s) for the author(s) of this article can be found under https://doi.org/10.1002/smll.202308925

DOI: 10.1002/smll.202308925

 © 2024 Wiley-VCH GmbH

stacking order to expand current knowledge regarding the III–VI family.

In this study, we present the synthesis of InTe via molecular beam epitaxy (MBE) growth on a graphene substrate, which offers a bottom–up approach for the fabrication of vertical heterostructures involving InTe. Our analysis technique mainly utilized atomic-resolution high-angle annular dark-field imaging-scanning transmission electron microscopy (HAADF-STEM) to determine the crystal structure and stacking orders of InTe. Our findings indicated that InTe has an unconventional stacking order and can be stabilized as a new polytype from III–VI metal monochalcogenide, with strong interlayer coupling demonstrated by the correlation between stacking modes and interlayer distances. Furthermore, we used ab initio density functional theory (DFT) calculations to describe the layer-by-layer MBE deposition process and discovered that the new stacking order formed along the deposition path with the lowest energy.

2. Results and Discussion

2.1. Polytypes of III–VI Metal Monochalcogenides

The monolayer structure of III–VI metal monochalcogenides is composed of two post-transition metal atoms (M) and two chalcogen atoms (X) covalently bonded in an X–M–M–X configuration, as illustrated in **Figure 1**. The top view of monolayer MX shows a hexagonal structure similar to the structure of conventional transition-metal dichalcogenides. Each layer of MX has a D_{3h} symmetry and consists of four atoms in the unit cell. In bulk form, MX can exist in four polytypes, designated β (2H)-, ϵ (2H′)-, δ (2H-3R)-, and γ (3R)-phases, as shown in Figure 1a. Although the results of various theoretical studies have suggested the potential for new polytypes, only β-, ϵ-, δ-, and γ-phases have been experimentally identified thus far. The β-, ϵ-, δ-, and γ-phases possess space groups of D^4_{6h}, D^1_{3h}, D^5_{3v}, and C^4_{6v}, respectively; among these phases, the β-, ϵ-, and δ-phases exhibit hexagonal structures, whereas the γ-phase displays a rhombohedral structure.

Considering that the stacking mode defines the polytype configuration, the polytypes of III–VI metal monochalcogenide can be described in terms of stacking mode, as classified in Figure 1b. By adopting the nomenclature proposed in,[27] stacking sequences of III–VI metal monochalcogenide can be classified into three high-symmetry patterns. The AA′ stacking type refers to alternate stacking of M and X atoms between layers, with M on top of X and vice versa; AB stacking corresponds to the stacking of M atoms directly above X atoms in the layer below. Additionally, AB′ stacking involves the stacking of M atoms above M atoms in the layer below. In summary, bilayer MX structures can adopt three stacking patterns with high symmetry: one eclipsed arrangement (AA′), and two staggered arrangements (AB and AB′). Among these, the AA′ stacking (β, 2H) and AB stacking (γ, 3R) patterns are commonly observed in both natural and synthesized samples.

As shown in Figure 1a, the previously identified polytypes have displayed only AA′ and AB stacking modes. In this study, we discovered that a new stacking mode (AB′ type) prevails in InTe. We have designated this novel polytype as the β'-phase ($P6_3/mmc$ space group), which is illustrated in Figure 1c with atomic-resolution imaging. The β'-phase involves the simplest case of AB′ stacking and exhibits the greatest symmetry with an inversion center. The unit cell comprises two layers of four In and four Te atoms.

2.2. Identification of InTe Crystal Structure

We synthesized InTe on graphene using an MBE process, where free-standing graphene served as a substrate supported by a SiN-membrane TEM grid, as shown in Figure S1 (Supporting Information). This approach enabled direct TEM observation of large areas of material grown after the MBE process. The resulting InTe material grew in the form of hexagon-pyramidal nanoparticles, suggesting that it possessed hexagonal symmetry as shown in **Figure 2a**. The hexagon-shaped nanoparticles had lateral lengths of ≈600 nm. Additionally, the pyramid shape of the grown InTe particles was confirmed through atomic force microscopy measurements and cross-sectional views, as shown in Figure S2a,b (Supporting Information).

The crystal structure of the grown InTe was investigated using atomic-resolution STEM imaging and energy dispersive X-ray (EDX) spectroscopy. EDX measurements showed that the In:Te elemental ratio was 1:1 (Figure S2(c), Supporting Information). Atomic-resolution HAADF-STEM images of plan-view InTe samples revealed a hexagonal crystal structure with a lattice parameter of 4.33 Å, as displayed in Figure 2b. Additionally, we observed various contrasts in atomic-resolution HAADF-STEM images along the [0001] zone axis, as shown in Figure S3 (Supporting Information). HAADF-STEM is a Z-contrast imaging technique; thus, its contrast is affected by the number and type of atoms constituting an atomic column. These findings suggest that InTe can have various stacked structures, which will be discussed later in more detail.

Importantly, crystal structure information from the flake side direction was obtained via cross-sectional TEM samples. HAADF-STEM imaging in Figure 2d–g visualized the layered crystal structure and stacking sequence. Atomic-resolution STEM imaging and EDX mapping revealed that each layer comprised a unit of four atoms arranged in a Te–In–In–Te sequence. Figure 2h presents a close-up view of the interfacial region between the InTe vdW layers and the graphene substrate; the layers displayed well-ordered characteristics during the initial growth stage, as indicated by the discernible structure near the substrate, including the vdW gaps that separated individual layers. The Te–In–In–Te bonds within a layer exhibited covalent interactions (strong intralayer interactions), whereas vdW interactions were present between layers. The inherent weakness of vdW interactions enabled the formation of multiple stacking sequences.

2.3. Three Types of Stacking Sequences and Their Interlayer Distances

We discovered that the majority of the grown InTe samples—previously unreported III–VI metal monochalcogenides—comprised AB′ stacking. The AB′ stacking sequence was located close to the graphene substrate and across the entire film thickness, as indicated in **Figures 3a** and S4 (Supporting Information). Thus, AB′ stacking was preferred, regardless of position

© 2024 Wiley-VCH GmbH

16136829, 0, Downloaded from https://onlinelibrary.wiley.com/doi/10.1002/smll.202308925 by Kyung Hee University Library, Wiley Online Library on [25/01/2024]. See the Terms and Conditions (https://onlinelibrary.wiley.com/terms-and-conditions) on Wiley Online Library for rules of use; OA articles are governed by the applicable Creative Commons License

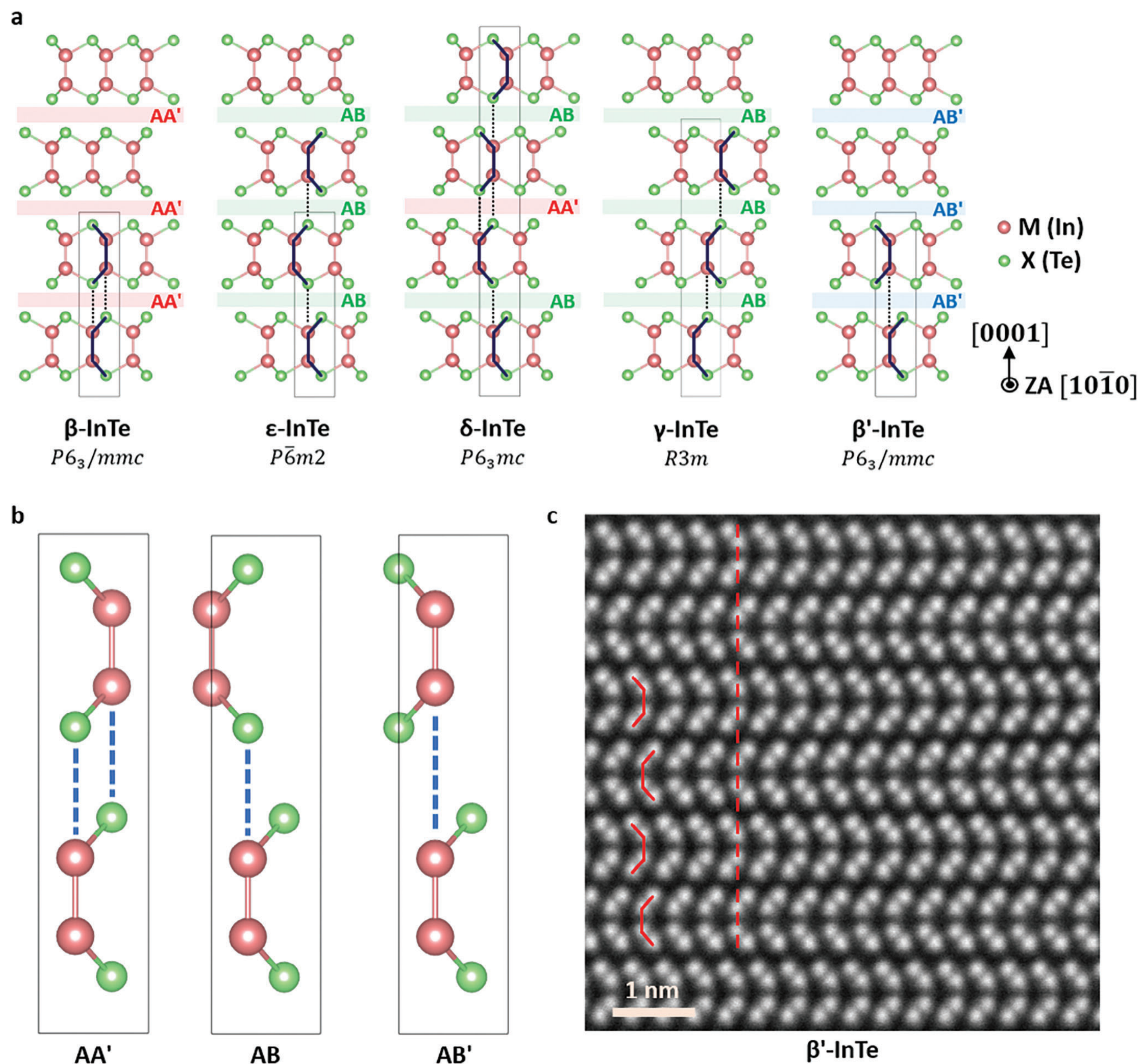

Figure 1. Polytypes of InTe. a) Schematic illustrations of the β, ϵ, δ, γ, and new β' polytypes of vdWlayered InTe. The stacking type is indicated for each interlayer. Red, green, and blue colors represent AA′, AB, and AB′ stacking, respectively. The β' polytype solely consists of AB′ stacking. b) Side views of the three possible high-symmetry stacking patterns in bilayer InTe. AB′ stacking forms one column of In atoms along the c-axis. c) Atomic-resolution HAADF-STEMimage of β'-InTe. The red solid line indicates Te–In–In–Te units in individual monolayers. The red dashed line represents the In atom column along the c-axis, which illustrates AB′ stacking.

during growth. In addition to the dominant AB′ stacking, other conventional stackings were present, as shown in Figure 3a. AA′ and AB stackings intervened, forming stacking faults between AB′ stacking structures (enlarged images in Figure 3b,c, respectively).

To quantify stacking types and understand the origins of stacking preferences, we scrutinized interlayer distances for each stacking type on the basis of atomic positions determined from atomic-resolution HAADF-STEM images. **Figure 4a** shows the interlayer distances for a representative image; the colored dots are overlaid on actual HAADF-STEM images to indicate the interlayer distance magnitude. This analysis shows that the interlayer distances differed according to stacking structure. To achieve robust statistics, we analyzed a large number of images with areas >5451 nm^2 (323 layers). Figure 4b shows the distribution of interlayer distances according to stacking structure, as three well-separated clusters. The leftmost cluster consisted of 7816 atoms, the middle cluster consisted of 4147 atoms, and the rightmost cluster consisted of 381 atoms; these cluster arrangements coincided with AB′, AB, and AA′ stacking, respectively. The data

 © 2024 Wiley-VCH GmbH

16136829, 0, Downloaded from https://onlinelibrary.wiley.com/doi/10.1002/smll.202308925 by Kyung Hee University Library, Wiley Online Library on [25/01/2024]. See the Terms and Conditions (https://onlinelibrary.wiley.com/terms-and-conditions) on Wiley Online Library for rules of use; OA articles are governed by the applicable Creative Commons License

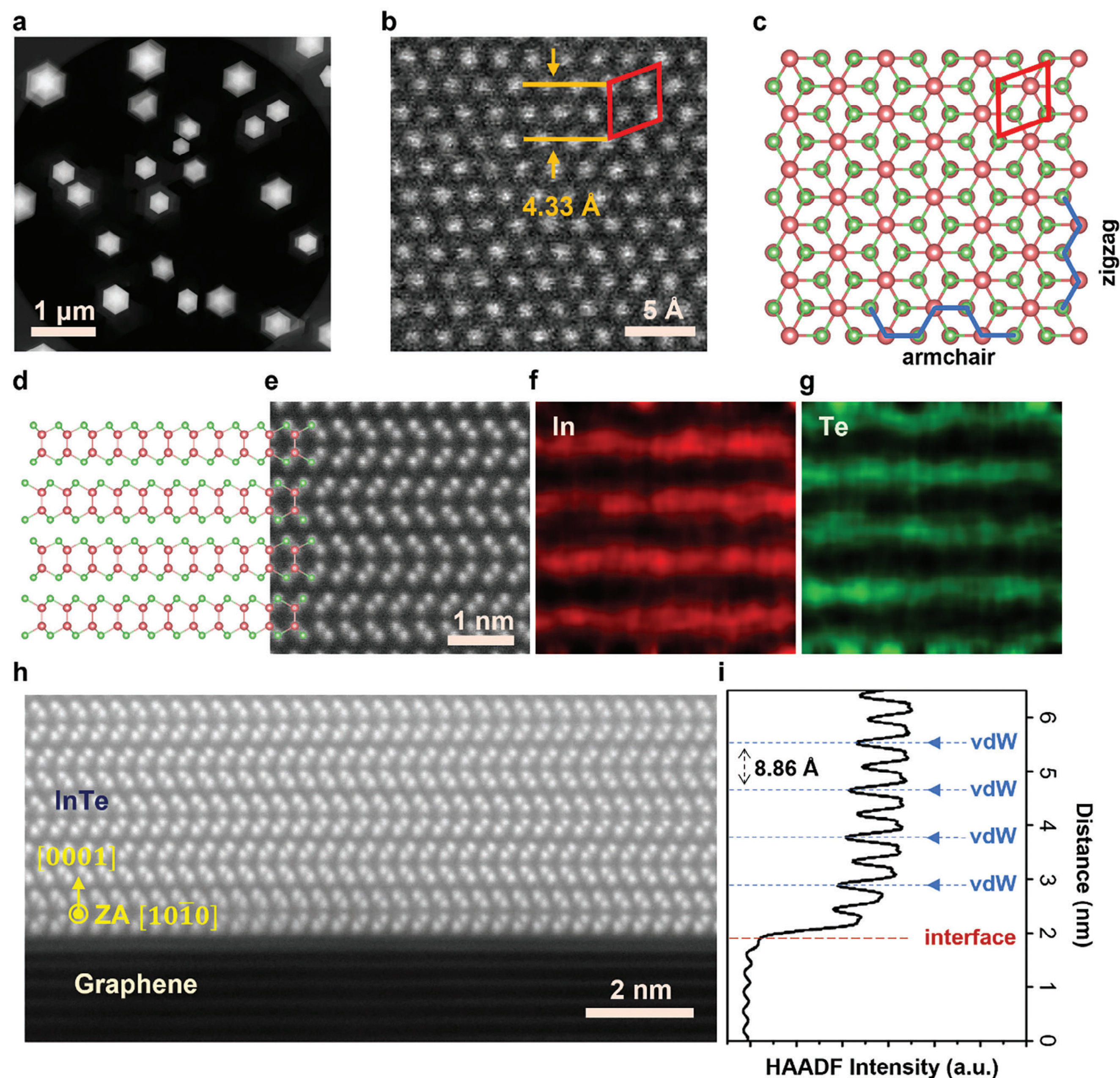

Figure 2. Identification of the InTe crystal structure. a) HAADF-STEM images of hexagonal pyramid-shaped InTe flakes on graphene. b) Atomic-resolution HAADF-STEM image of InTe along the [0001] zone axis and c) its atomic model. The red rhombus represents the unit cell of InTe. d,e) Atomic model of InTe along the [10$\bar{1}$0] zone axis overlaid on HAADF-STEM image of InTe. f,g) STEM-EDX mapping data for the location shown in panel (e). The red element is In, and the green element is Te. These data illustrate a monolayer structure in which Te surrounds In. h) HAADF-STEM image of the interface and i) its line profile for intensity along the [0001] direction. Each interlayer exhibits a low intensity, which corresponds to the vdW gap.

showed that AA′ stacking was rare, AB stacking was the second most common type, and AB′ stacking was the most common type (Figure 4b). Therefore, we concluded that InTe prefers the AB′ stacking sequence. Furthermore, interlayer distances were strongly correlated with stacking type occurrence. According to stacking group, the interlayer distances were 8.86 Å, 8.93 Å, and 9.00 Å for AB′, AB, and AA′ stacking, respectively. AB′ stacking, the most prominent stacking sequence, had the shortest interlayer distance. Considering that the short distance between vdW layers implies strong coupling, AB′ stacking allows the most stable and dominant structure. Thus, for InTe, formation of the β'-phase consisting of only AB′ stacking may be preferred.

To better understand the origin of the preference for AB′ stacking, ab initio DFT calculations were performed. We compared interlayer distances according to stacking type. The DFT calculations revealed that AB′ stacking had the shortest interlayer distance, consistent with experimental results (Figure S5, Supporting Information). Additionally, among all stackings, the

© 2024 Wiley-VCH GmbH

16136829, 0, Downloaded from https://onlinelibrary.wiley.com/doi/10.1002/smll.202308925 by Kyung Hee University Library, Wiley Online Library on [25/01/2024]. See the Terms and Conditions (https://onlinelibrary.wiley.com/terms-and-conditions) on Wiley Online Library for rules of use; OA articles are governed by the applicable Creative Commons License

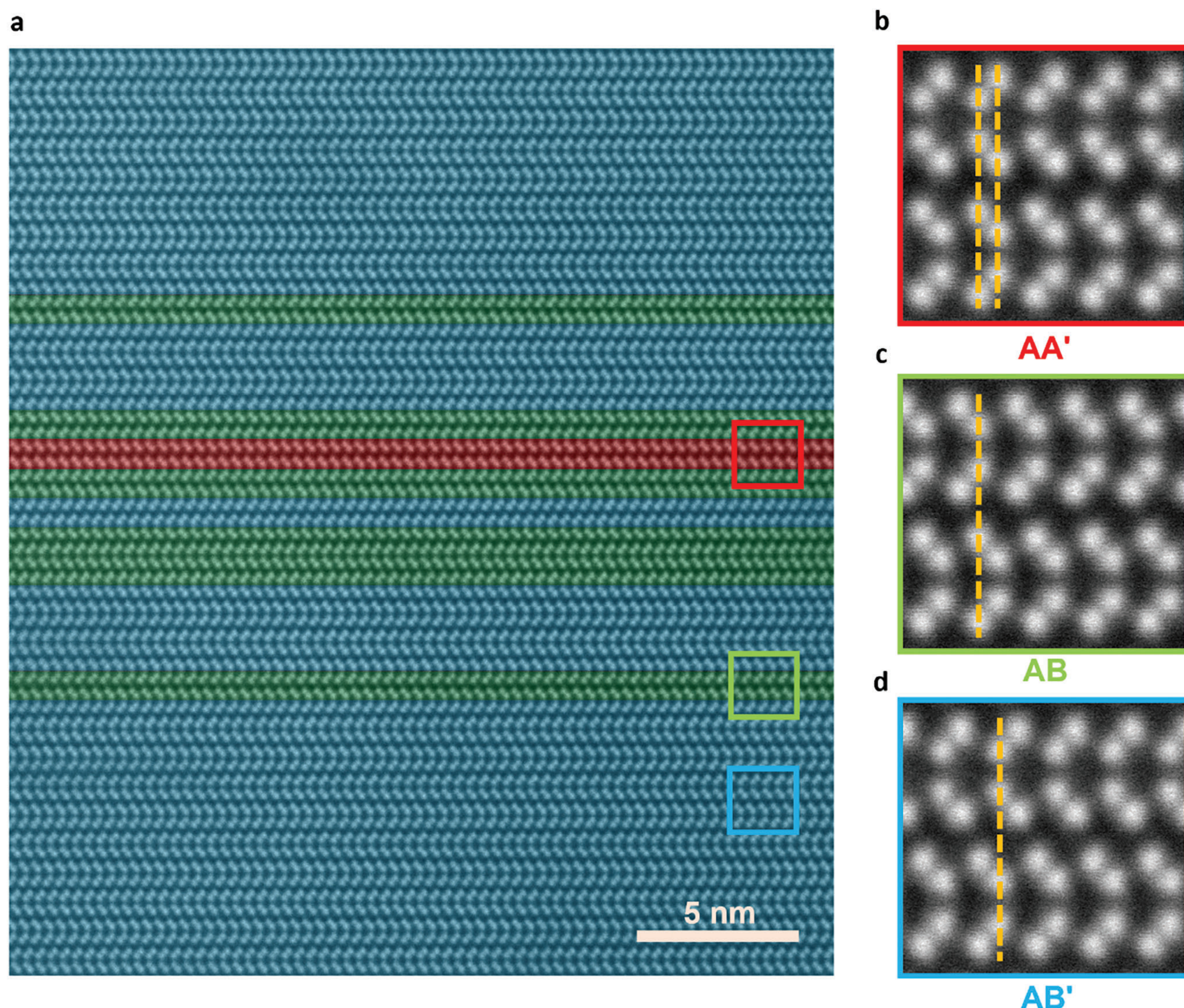

Figure 3. Stacking patterns of InTe. a) Atomic-resolution HAADF-STEM image with stacking sequences identified. The red, green, and blue regions represent AA′, AB, and AB′ stacking, respectively. Most of the area displays AB′ stacking. b–d) Enlarged image of the red (b), green (c), and blue (d) squares in (a), which correspond to AA′, AB, and AB′ stacking, respectively. Yellow dashed lines guide atomic columns that distinguish each stacking type.

interlayer vdW bonding of AB′ stacking resulted in the greatest change in electron density localized in the interlayer region, as shown in Figure S5 (Supporting Information). Thus, stronger interlayer coupling occurred in the AB′ stacking configuration.

2.4. Origin of AB′ Stacking Dominance in the Molecular Beam Epitaxy Process

The MBE process is governed by surface interactions between evaporated beams and the outermost atomic layer, leading to layer-by-layer assembly.[28] Thus, to adjust for the layer-by-layer MBE epitaxial growth, the binding energy of the Te layer on top of the InTe monolayer was evaluated as shown in **Figure** 5a,b. Two highly symmetric configurations were compared. In the first configuration, Te atoms were deposited over the hexagonal center of the InTe monolayer; in the second configuration, they were vertically aligned on the In atom site of the InTe monolayer. The first configuration was much more stable than the second configuration, suggesting that Te strongly favors a specific position on top of the InTe monolayer. Subsequently, the binding energy of the In layer on Te plus the InTe monolayer was determined, as illustrated in Figure 5c–f. In this step, the stacking type was determined according to the position of In layer deposition. Comparison of the binding energies in each case showed that AB′ stacking was preferred over AB stacking in the first configuration; AB stacking was more advantageous than AA′ stacking in the second configuration. Overall, use of the route with the lowest energy leads to AB′ stacking; the opposite route results in AA′ stacking with the highest energy. Importantly, energy differences among

© 2024 Wiley-VCH GmbH

16136829, 0, Downloaded from https://onlinelibrary.wiley.com/doi/10.1002/smll.202308925 by Kyung Hee University Library, Wiley Online Library on [25/01/2024]. See the Terms and Conditions (https://onlinelibrary.wiley.com/terms-and-conditions) on Wiley Online Library for rules of use; OA articles are governed by the applicable Creative Commons License

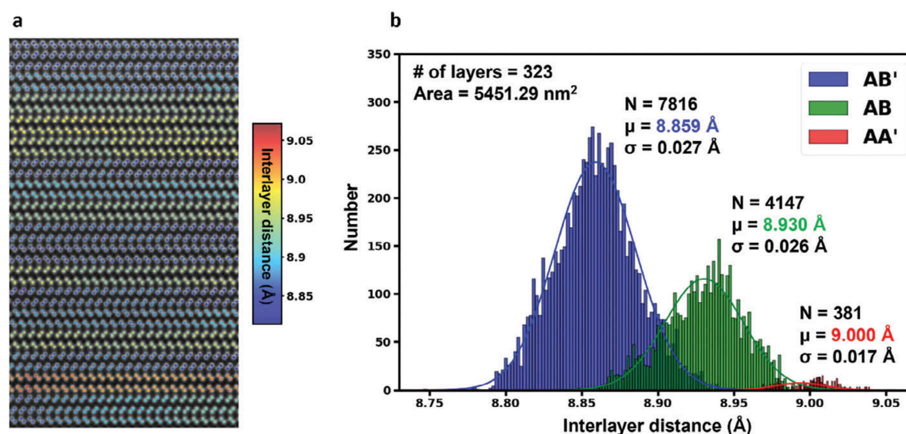

Figure 4. Stacking modes and interlayer distances. a) Atom positions overlaid on the HAADF-STEM image, with each color corresponding to the interlayer distances in Å. To display the upper and lower interlayer separately, the In–Te–Te–In monolayer was divided into the upper In–Te half sublayer and the lower Te–In half sublayer. The upper interlayer distance is colored in the upper In–Te half sublayer; the lower interlayer distance is colored in the lower Te–In half sublayer. Peak position refinement with a 2D Gaussian function was performed to measure the positions of the atoms; the atom positions were subsequently used to quantify the interlayer distances. b) Distribution of interlayer distance according to stacking mode. Blue, green, and red bars correspond to the observed numbers of AB′, AB, and AA′ stackings, respectively. AB′ stacking is the most abundant and has the shortest interlayer distance.

the three structures were much smaller (Figure S5, Supporting Information). This finding implies that even when all stackings are energetically stable, the pathway ultimately favors a specific stacking configuration. Therefore, we propose that AB′ stacking dominance arises from the layer-by-layer MBE epitaxial growth. Accordingly, when the growth occurs in a layer-by-layer manner, the atoms deposited at each step prefer a specific position on the already grown product. Thus, AB′ stacking provided the most energetically preferred path.

The layer-by-layer MBE epitaxial growth is also strongly supported by the presence of a certain type of AB stacking. There are two types of AB stacking when the growth direction is important, because there are two paths that lead to AB stacking. One path is derived from the first configuration, and the other path originates from the second configuration, as shown in Figure 5h,i. To distinguish these paths, we designated them γ-type AB stacking and ϵ-type AB stacking, respectively. One stacking type becomes the other type when flipped; thus, the two types of AB stacking are considered equivalent. However, if the energy difference is sufficiently large with respect to the growth direction, the temporal stacking sequence is important and the preference for the two AB stackings differs. It is clear that γ-type AB stacking forms a sequence of energetically much more favorable pathways, compared with ϵ-type AB stacking. Indeed, as revealed by the representative image and statistics in Figure S6 (Supporting Information), most AB stackings display the γ-type and only a few display the ϵ-type. Thus, although both γ- and ϵ-phases consist solely of AB stacking, the preference for the γ-phase over the ϵ-phase arises because the ϵ-phase requires energetically unfavorable ϵ-type AB stacking. Additionally, the pattern of the γ-phase is dominated by γ-type AB stacking (rather than ϵ-type AB stacking), as shown in Figure S7 (Supporting Information). Therefore, the imbalance of the two AB stackings strongly supports the layer-by-layer MBE epitaxial growth, which is the underlying mechanism for AB′ stacking or β'-phase dominance.

3. Conclusion

We utilized MBE to grow InTe on graphene, then examined its crystal structure and stacking sequences using atomic-resolution STEM measurements. InTe with a hexagonal honeycomb lattice was realized; further evaluation revealed the prevalence of the AB′ stacking mode. Additionally, we directly measured the interlayer distance of the vdW gap and found a strong correlation between stacking sequence population and interlayer distance. A shorter interlayer distance was associated with the presence of additional stacking sequences, highlighting the strong coupling of the AB′ stacking configuration and the stability of the novel polytype β'-phase. Our results indicate that MBE is a viable method for synthesizing the new centrosymmetric polytype of the III–VI family; they suggest the potential for exploring novel 2D materials with diverse polytypic characteristics.

4. Experimental Section

InTe Synthesis: Epitaxial growth of InTe was performed using a custom-designed ultra-high vacuum MBE system. Growth details are present in Figure S1(b) (Supporting Information). Indium and tellurium atoms were sourced from their respective effusion cells at different stages of the growth procedure. Initially, substrates or templates were prepared by mechanical exfoliation of single-crystalline graphene flakes onto SiN-membrane TEM grids. These substrates were then loaded into the growth chamber, where thermal cleaning was conducted under ultra-high vacuum conditions at 550 °C for 30 min. High-purity elemental sources with In (99.999%) and Te (99.999%) were used; the chamber base pressure was maintained at $\approx 10^{-10}$ Torr. Indium and tellurium were evaporated using Knudsen cells. The In flux was supplied at ≈850 °C with a rate of ≈0.03 Å s^{-1}. The Te flux was 16–18-fold higher than the In flux and was continuously supplied throughout the growth process at 300 °C.

Characterizations: Cross-sectional STEM samples were fabricated using focused ion beam milling with an FEI Helios 650 focused ion beam system (FEI Company, Hillsboro, OR, USA), followed by additional

 © 2024 Wiley-VCH GmbH

16136829, 0, Downloaded from https://onlinelibrary.wiley.com/doi/10.1002/smll.202308925 by Kyung Hee University Library, Wiley Online Library on [25/01/2024]. See the Terms and Conditions (https://onlinelibrary.wiley.com/terms-and-conditions) on Wiley Online Library for rules of use; OA articles are governed by the applicable Creative Commons License

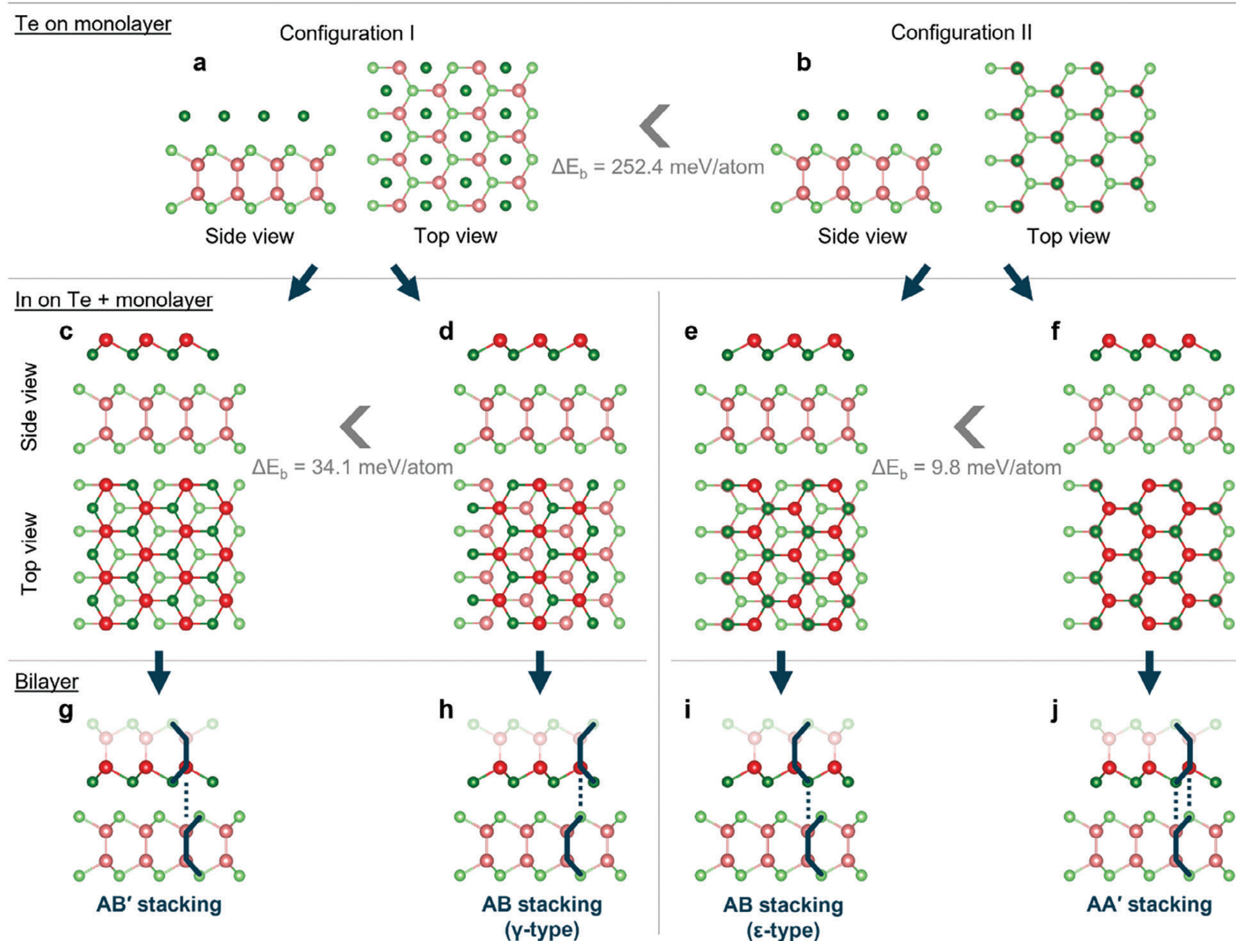

Figure 5. Binding energy of atoms deposited at each step during layer-by-layer growth. a,b) Two configurations where Te is deposited on a InTe monolayer. Deposited Te atoms are displayed in dark green. Te can be placed above the hexagon center or in the In column position of the monolayer. The first configuration is considerably more stable than the second. c–f) The deposition of In on the Te + InTe monolayer leads to each stacking type. Dark red atoms represent deposited In atoms. g–j) Bilayers at the final stage when grown in a layer-by-layer manner. Use of the most energetically stable path leads to AB′ stacking, whereas the opposite path leads to AA′ stacking. AB stacking is further classified into two cases according to growth direction: γ-type and ϵ-type. The γ-type is achieved through an energetically favored pathway over the ϵ-type.

thinning via focused Ar-ion milling with a Fischione NanoMill 1040 (E.A. Fischione Instruments, Inc., Export, PA, USA). STEM images were captured using a Thermo Fisher Scientific Themis Z aberration-corrected microscope (Thermo Fisher Scientific, Waltham, MA, USA), operating at a primary beam energy of 200 kV. The imaging setup included a semi-convergence angle of 18.2 mrad and an HAADF detector with an angular range of 70–200 mrad (camera length: 115 mm). To improve the signal-to-noise ratio, a series of 10 images (4096 × 4096 pixels; 2 µs dwell time) were recorded and cross-correlated.[29] The positions of atomic columns were determined by iteratively fitting them to a 2D Gaussian function, enabling precise displacement measurements with picometer accuracy in adjacent layers.[30]

Ab Initio Density Functional Calculations: The DFT within the generalized gradient approximation was used for ab initio calculations with the Vienna ab initio simulation package.[31] The semiempirical Grimme's DFT-3 method[32] was implemented to adjust for van der Waals interactions. Optimization of the lattice parameters and atomic positions was conducted until the forces on each atom reached a value of <0.01 eV Å^{-1}. To prevent spurious interactions between adjacent slabs, a vacuum layer of >20 Å was employed. Brillouin zone sampling was conducted using a 15 × 15 × 1 k-point mesh based on the Monkhorst–Pack scheme.[33]

Supporting Information

Supporting Information is available from the Wiley Online Library or from the author.

Acknowledgements

This work was supported by the National Research Foundation of Korea (NRF) grant funded by the Korea government (NRF-2022R1A2C3007807, NRF-2019M3D1A1079215, NRF-2022R1A2C1005505, NRF-2022M3F-3A2A01073562, and NRF- 2021R1A5A1032996).

Conflict of Interest

The authors declare no conflict of interest.

Data Availability Statement

The data that support the findings of this study are available from the corresponding author upon reasonable request.

© 2024 Wiley-VCH GmbH

16136829, 0, Downloaded from https://onlinelibrary.wiley.com/doi/10.1002/smll.202308925 by Kyung Hee University Library, Wiley Online Library on [25/01/2024]. See the Terms and Conditions (https://onlinelibrary.wiley.com/terms-and-conditions) on Wiley Online Library for rules of use; OA articles are governed by the applicable Creative Commons License

Keywords

III–VI metal chalcogenides, indium telluride, molecular beam epitaxy, scanning transmission electron microscopy, van der Waals layered materials

Received: October 6, 2023
Revised: December 7, 2023
Published online:

[1] M. Aoki, H. Amawashi, *Solid State Commun.* **2007**, *142*, 123.
[2] G. Constantinescu, A. Kuc, T. Heine, *Phys. Rev. Lett.* **2013**, *111*, 036104.
[3] H. Luo, W. Xie, J. Tao, H. Inoue, A. Gyenis, J. W. Krizan, A. Yazdani, Y. Zhu, R. J. Cava, *Proc. Natl. Acad. Sci. U.S.A.* **2015**, *112*, E1174.
[4] S. Deckoff-Jones, J. Zhang, C. E. Petoukhoff, M. K. L. Man, S. Lei, R. Vajtai, P. M. Ajayan, D. Talbayev, J. Madéo, K. M. Dani, *Sci. Rep.* **2016**, *6*, 22620.
[5] W. Bao, L. Jing, J. Velasco, Y. Lee, G. Liu, D. Tran, B. Standley, M. Aykol, S. B. Cronin, D. Smirnov, M. Koshino, E. Mccann, M. Bockrath, C. N. Lau, *Nat. Phys.* **2011**, *7*, 948.
[6] C. H. Lui, Z. Li, K. F. Mak, E. Cappelluti, T. F. Heinz, *Nat. Phys.* **2011**, *7*, 944.
[7] X. Zhou, J. Cheng, Y. Zhou, T. Cao, H. Hong, Z. Liao, S. Wu, H. Peng, K. Liu, D. Yu, *J. Am. Chem. Soc.* **2015**, *137*, 7994.
[8] K. A. Mengle, E. Kioupakis, *APL Mater.* **2019**, *7*, 021106.
[9] Y.u. F. Solomonov, V. K. Subashiev, *Phys. Status Solidi A* **1982**, *74*, 75.
[10] W. Shi, Y. J. Ding, N. Fernelius, K. Vodopyanov, *Opt. Lett.* **2002**, *27*, 1454.
[11] J. Zhou, J. Shi, Q. Zeng, Y. Chen, L. Niu, F. Liu, T. Yu, K. Suenaga, X. Liu, J. Lin, Z. Liu, *2D Mater.* **2018**, *5*, 025019.
[12] M. Miao, J. Botana, E. Zurek, T. Hu, J. Liu, W. Yang, *Chem. Mater.* **2016**, *28*, 1994.
[13] D. A. Bandurin, A. V. Tyurnina, G. L. Yu, A. Mishchenko, V. Zólyomi, S. V. Morozov, R. K. Kumar, R. V. Gorbachev, Z. R. Kudrynskyi, S. Pezzini, Z. D. Kovalyuk, U. Zeitler, K. S. Novoselov, A. Patanè, L. Eaves, I. V. Grigorieva, V. I. Fal'ko, A. K. Geim, Y. Cao, *Nat. Nanotechnol.* **2017**, *12*, 223.
[14] J. Chen, X. He, B. Sa, J. Zhou, C. Xu, C. Wen, Z. Sun, *Nanoscale* **2019**, *11*, 6431.
[15] H. L. Zhuang, R. G. Hennig, *Chem. Mater.* **2013**, *25*, 3232.
[16] N. Leisgang, J. G. Roch, G. Froehlicher, M. Hamer, D. Terry, R. Gorbachev, R. J. Warburton, *AIP Adv.* **2018**, *8*, 105120.
[17] A. Kuhn, A. Chevy, R. Chevalier, *Phys. Status Solidi A* **1975**, *31*, 469.
[18] J. Srour, M. Badawi, F. El Haj Hassan, A. Postnikov, *J. Chem. Phys.* **2018**, *149*, 054106.
[19] V. Zólyomi, N. D. Drummond, V. I. Fal'ko, *Phys. Rev. B* **2014**, *89*, 205416.
[20] S. Demirci, N. Avazli, E. Durgun, S. Cahangirov, *Phys. Rev. B* **2017**, *95*, 115409.
[21] A. V. Matetskiy, V. V. Mararov, A. N. Mihalyuk, N. V. Denisov, S. V. Eremeev, A. V. Zotov, A. A. Saranin, *Phys. Rev. B* **2022**, *106*, 165301.
[22] G. Tan, W. G. Zeier, F. Shi, P. Wang, G. J. Snyder, V. P. Dravid, M. G. Kanatzidis, *Chem. Mater.* **2015**, *27*, 7801.
[23] P. Mannu, M. Palanisamy, G. Bangaru, S. Ramakrishnan, M. Ramcharan, A. Kandasami, *AIP Adv.* **2018**, *8*, 115015.
[24] S. Misra, A. Léon, P. Levinský, J. Hejtmánek, B. Lenoir, C. Candolfi, *J. Mater. Chem. C* **2021**, *9*, 14490.
[25] J. Feng, M. Zhou, J. Li, G. Dong, S. Gao, E. Min, C. Zhang, J. He, R. Sun, R. Liu, *Mater. Horiz.* **2023**, *10*, 3082.
[26] S. Lee, M. Kim, Y.-K. Kwon, *npj 2D Mater. Appl.* **2023**, *7*, 43.
[27] L. Liang, A. A. Puretzky, B. G. Sumpter, V. Meunier, *Nanoscale* **2017**, *9*, 15340.
[28] D. G. Schlom, L.-Q. Chen, X. Pan, A. Schmehl, M. A. Zurbuchen, *J. Am. Ceram. Soc.* **2008**, *91*, 2429.
[29] B. H. Savitzky, I. El Baggari, C. B. Clement, E. Waite, B. H. Goodge, D. J. Baek, J. P. Sheckelton, C. Pasco, H. Nair, N. J. Schreiber, J. Hoffman, A. S. Admasu, J. Kim, S.-W. Cheong, A. Bhattacharya, D. G. Schlom, T. M. Mcqueen, R. Hovden, L. F. Kourkoutis, *Ultramicroscopy* **2018**, *191*, 56.
[30] H. Kim, J. Y. Zhang, S. Raghavan, S. Stemmer, *Phys. Rev. X* **2016**, *6*, 041063.
[31] G. Kresse, J. Furthmüller, *Phys. Rev. B* **1996**, *54*, 11169.
[32] S. Grimme, J. Antony, S. Ehrlich, H. Krieg, *J. Chem. Phys.* **2010**, *132*, 154104.
[33] H. J. Monkhorst, J. D. Pack, *Phys. Rev. B* **1976**, *13*, 5188.

© 2024 Wiley-VCH GmbH

16136829, 0, Downloaded from https://onlinelibrary.wiley.com/doi/10.1002/smll.202308925 by Kyung Hee University Library, Wiley Online Library on [25/01/2024]. See the Terms and Conditions (https://onlinelibrary.wiley.com/terms-and-conditions) on Wiley Online Library for rules of use; OA articles are governed by the applicable Creative Commons License